11. HIGH-RESOLUTION SCANNING ELECTRON MICROSCOPY

JINGYUE LIU

1. INTRODUCTION: SCANNING ELECTRON MICROSCOPY AND NANOTECHNOLOGY

Ultimately, all materials, organic or inorganic, have their origins in the collective assembly of a small number of atoms or molecules. Human beings have been fascinated by the interior world: the secrets of cells and the building blocks of matter. Ever since various types of microscopes were discovered, they have been the primary instruments for helping us to directly observe, understand, and manipulate matter or cells on an ever-decreasing scale. By understanding what the building blocks are and how they are arranged together to form architectures that possess unique properties or display specific functions, we hope to modify, manipulate, and sculpt matter at nanoscopic dimensions for desired purposes. To understand the fundamental properties of various nanosystems, it is necessary to characterize their structures at a nanometer or atomic level and integrate the nanoscale components that provide macroscale functions or properties. This, in turn, allows us to understand the synthesis-structure-property relationships of nanosystems, thus achieving the ultimate goal of molecular engineering of functional systems.

The scanning electron microscope (SEM) is undoubtedly the most widely used of all electron beam instruments. The popularity of the SEM can be attributed to many factors: the versatility of its various modes of imaging, the excellent spatial resolution now achievable, the very modest requirement on sample preparation and condition, the relatively straightforward interpretation of the acquired images, the accessibility of associated spectroscopy and diffraction techniques. And most importantly its

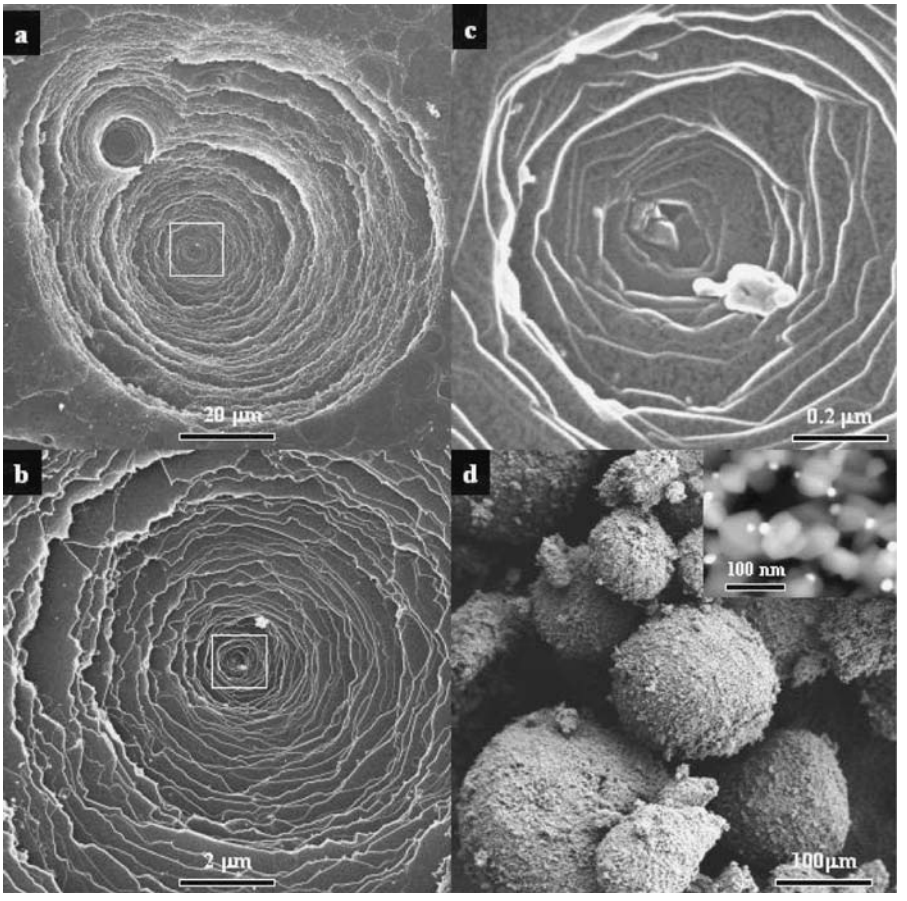

Figure 1. Secondary electron images of a Pt/graphite system showing the surface morphology at low magnification (a), medium magnification (b) and high magnification (c); low magnification secondary electron image (d) of a Pd/TiO_2 catalyst showing the general morphology of the catalyst powders and high-resolution backscattered electron image (inset) showing the size and morphology of the Pd and TiO_2 nanoparticles.

user-friendliness, high levels of automation, and high throughput make it accessible to most research scientists. With the recent generation of SEM instruments, high-quality images can be obtained with an image magnification as low as about 5× and as high as >1,000,000×; this wide range of image magnifications bridges our visualization ability from naked eyes to nanometer dimensions. Image resolution of about 0.5 nm can now be achieved in the most recent generation field-emission-gun SEM (FEG-SEM), clearly rivaling that of a transmission electron microscope (TEM); the sample size, however, can be as large as production-scale silicon wafers.

As an example, Fig. 1 shows a set of images that demonstrate the usefulness of correlating low magnification images to high-resolution images. Figure 1a shows a low

magnification secondary electron (SE) image of an annealed Pt/graphite sample. The sample was prepared by sputtering Pt nanoparticles onto freshly cleaved graphite surface and then the Pt/graphite composite was annealed at 900°C in a flowing mixture of N_2 and H_2 for 10 hours. The purpose was to study the dependence of Pt-graphite interaction processes on the gas environment, annealing temperature, and residence time. Figure 1a and many other images clearly showed that many large pits had been generated on the graphite surface during the annealing process. Medium magnification images such as the one shown in Fig. 1b revealed the presence of many surface steps, terraces, and the presence of some small particles within the pits. High-resolution images such as the one shown in Fig. 1c not only showed the size and shape of some nanoparticles residing on the graphite terraces and steps but also showed the step structure and the fine details on the graphite terraces. By analyzing these SE images and the corresponding X-ray energy dispersive spectroscopy (XEDS) data, information about the interaction processes between Pt nanoparticles and the graphite substrate and how the gas environment affects these processes can be extracted. Figure 1d shows another example of extracting useful information on nanostructured Pd/TiO_2 catalyst, which has important industrial applications. Nanoscale features on the catalyst beads can be easily obtained by zooming the magnification of the region of interest; and Pd nanoparticles can be easily identified in high-resolution backscattered electron (BE) images such as the one shown in the inset of Fig. 1d. Not only the size and spatial distribution of the Pd nanoparticles can be determined but also their spatial relationship to the TiO_2 nanocrystals can be extracted.

The SEM had its origins in the work of Knoll [1] and von Andenne [2, 3]; images of surfaces with material, topographic, and crystallographic contrast were obtained [4]. The first modern SEM, however, was described by Zworykin *et al.* [5]; the instrument incorporated most of the features of a current SEM such as a secondary electron detector and a cathode-ray-tube display, achieving an image resolution of about 5 nm on solid specimens. The aggressive development of the various components of a modern SEM by the Oatley group at Cambridge University led to the first commercial production of the SEM [6].

The introduction of the use of a field-emission gun (FEG) in a scanning electron microscope made it possible to image individual heavy atoms in the transmission mode by collecting scattered electrons with an annular detector [7–9]. The wide use of the field-emission guns in the commercial SEM during the 1980s and 1990s, the significant improvement in the design of the probe-forming lens, the development of new detection schemes and detectors, and the revival of the development of high-resolution SE imaging in this time frame established the current practice and understanding of the high-resolution SEM techniques [10–20]. The continuous improvement in the field-emission guns, the probe forming lenses, the efficiency of various detectors, the automation of sample stages, and the digital image acquisition systems has made the modern high-resolution FEG-SEM a powerful and high-throughput tool for examining the physicochemical properties of a plethora of inorganic materials and biological systems on a nanometer scale.

The development of low-voltage SEM (LV-SEM) clearly broadened the application of the SEM techniques to non-conducting or delicate specimens; LV-SEM is now

the preferred mode of operation [20–23]. Although low-voltage SEM was not a new concept [1, 5] nanometer scale resolution is achievable only in the modern FEG-SEM; nanometer scale surface features of bulk samples is now obtainable with primary electron energies <1 keV. The significant reduction in the electron-specimen interaction volume clearly makes low-voltage SEM more surface-sensitive; and the charge balance at the specimen surface makes it possible to directly observe non-conducting materials without a conductive coating layer.

A very recent development is the use of a retarding field to modulate the landing energy of the primary electrons. By simply applying a negative potential to the specimen, a retarding field can be generated between the specimen and a grounded electrode just above the specimen; with this arrangement the specimen itself is part of a "cathode lens" system and high-resolution images can be obtained with ultra-low-energy electrons [24–25]. The use of primary electrons with a landing energy below 100 eV significantly enhances the surface sensitivity and greatly reduces the electron-beam-induced irradiation effects. With further improvement of low-voltage FEG-SEM optical systems the ultra-low-voltage SEM (ULV-SEM) technique will become a powerful tool for studying nanoscale systems.

The combination of a high-performance thermal FEG with improved condenser lens designs can produce electron nanoprobes with high stability and high probe-current, thus enabling various signals generated from the specimen to be collected with good signal-to-noise ratio. The incorporation of a high-sensitivity detector for collecting electron backscatter diffraction patterns (EBSP) allows lattice orientations of crystalline materials to be measured at each pixel and thus orientation images of individual grains can be formed. The incorporation of high-efficiency spectrometers makes it possible to perform high spatial resolution chemical microanalysis by XEDS [22–23] and wavelength dispersive spectroscopy (WDS) techniques.

Among many characterization techniques, microscopy should and will play an important role in understanding the nature of nanosystems. Microscopy and the associated analytical techniques can provide information on the physicochemical properties of individual nanocomponents as well as the spatial relationships among these nanocomponents. Among many microscopy techniques that are discussed in this volume, SEM techniques are unique in the sense that almost any sample can be examined in a modern, variable pressure or environmental FEG-SEM [26–29]; powders, films, pellets, conducting, semiconduing, non-conducting, "dirty", hydrated, and even wet samples can be examined with high spatial resolution and high image quality. Another advantage of the SEM is the amount of materials that can be examined: from macroscale such as pellets, powders, films, or even whole silicon wafers to nanoscale such as carbon nanotubes, metal nanoparticles, ceramic nanopowders, or nanoscale networks in polymers and fibers. The ability to quickly correlate the observations of nanostructures to macroscale properties is invaluable for providing statistically meaningful data in developing nanostructured systems.

The modern high-resolution FEG-SEM and associated techniques are suitable for applications to both the materials and life sciences. For example, it can be used in the automotive industry for metallurgy applications, in the chemical industry for

polymer and catalyst applications, in the semiconductor industry for device applications, in the food industry for particle and morphological applications, in the consumer health industry for nano-particulate applications, and in the pharmaceutical industry for drug and drug delivery applications. With the use of a low temperature system, fully hydrated biological systems can be examined at high spatial resolution providing morphological and ultrastructural information. With the rapid development of the computer technology and automated operations, live SEM images are now used in classroom lectures or are observed by scientists located at remote sites; telemicroscopy is now a reality.

Although there are many imaging, diffraction, and spectroscopic techniques available in the modern FEG-SEM, we review, in this chapter, only the recent development of high-resolution imaging techniques and the applications of these techniques to studying various types of nanophase materials. Interested readers should consult the existing textbooks for more detailed discussions on the fundamentals of SEM and related techniques [30–31]. This chapter is closely related to the chapters in this volume by D. Newberry on high-resolution quantitative chemical microanalysis, by J. Michael on EBSP and orientation imaging microscopy, and by J. M. Cowley on scanning transmission electron microscopy.

2. ELECTRON-SPECIMEN INTERACTIONS

When an electron beam interacts with a bulk specimen, a variety of electron, photon, phonon, and other signals can be generated (Fig. 2). There are three types of electrons that can be emitted from the electron-entrance surface of the specimen: secondary electrons with energies <50 eV, Auger electrons produced by the decay of the excited atoms, and backscattered electrons that have energies close to those of the incident electrons. All these signals can be used to form images or diffraction patterns of the specimen or can be analyzed to provide spectroscopic information. The de-excitation of atoms that are excited by the primary electrons also produces continuous and characteristic X-rays as well as visible light. These signals can be utilized to provide qualitative, semi-quantitative, or quantitative information on the elements or phases present in the regions of interest. All these signals are the product of strong electron-specimen interactions, which depends on the energy of the incident electrons and the nature of the specimen.

2.1. Electron-Specimen Interactions in Homogeneous Materials

Both elastic and inelastic scattering processes critically depend on the energy of the incident electrons. In a SEM instrument, the elastic and inelastic mean-free-paths of the primary electrons rapidly decrease with decreasing energy. Both the electron range, which is a measure of the penetration depth of the incident electrons, and the interaction volume, which is a measure of the diffusion of the incident electrons, are significantly reduced at low energies. By performing Monte Carlo simulations of the electron cascading processes inside a specimen, the energy dependence of the change in

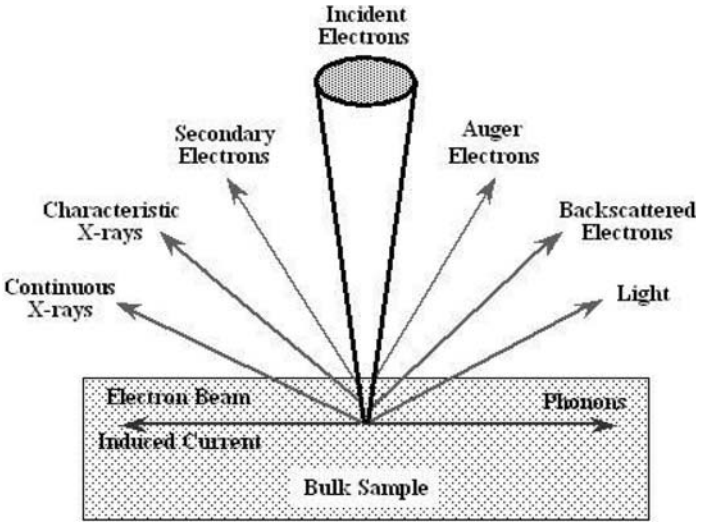

Figure 2. Schematic drawing illustrates the signals generated inside a scanning electron microscope when an electron beam interacts with a specimen.

the interaction volume, the yields of secondary electrons and backscattered electrons, and the penetration depth can be demonstrated [32].

As an example, Fig. 3 shows trajectories of incident electrons in bulk carbon and platinum for electrons with energies of 1 keV and 15 keV, respectively. In low atomic-number (Z) materials such as carbon, a large fraction of the high-energy electrons is scattered through small angles and subsequent electron diffusion results in a pear-shaped spatial distribution (Fig. 3b). In high-Z materials such as platinum, large-angle scattering events are enhanced and thus the electron trajectories are more strongly coiled up (Fig. 3d), reducing the penetration of the primary electrons into the sample. At low voltages, the differences in electron range between low-Z and high-Z materials, although still appreciable, are considerably reduced. For low-Z materials such as carbon, alumina, or silica, the electron interaction volume is reduced by five to six orders of magnitude from 15 keV to 1 keV. The corresponding electron range decreases by about 100 times. For high-Z materials such as platinum, gold, or tungsten, however, the decrease in the electron range and the interaction volume is not as drastic as that for low-Z materials. It is interesting to note that the range of 1-keV electrons in bulk platinum is less than about 10 nm.

Figure 3 also shows that at higher energies there are significant differences in the electron range and interaction volume between low-Z and high-Z materials. At lower energies, however, these differences rapidly diminish. At electron energies <0.5 keV, all materials have approximately the same range and interaction volume. At ultra-low electron energies (<100 eV), surface scattering may play a significant role in determining the nature of the electron-specimen interactions. The imaging theory of

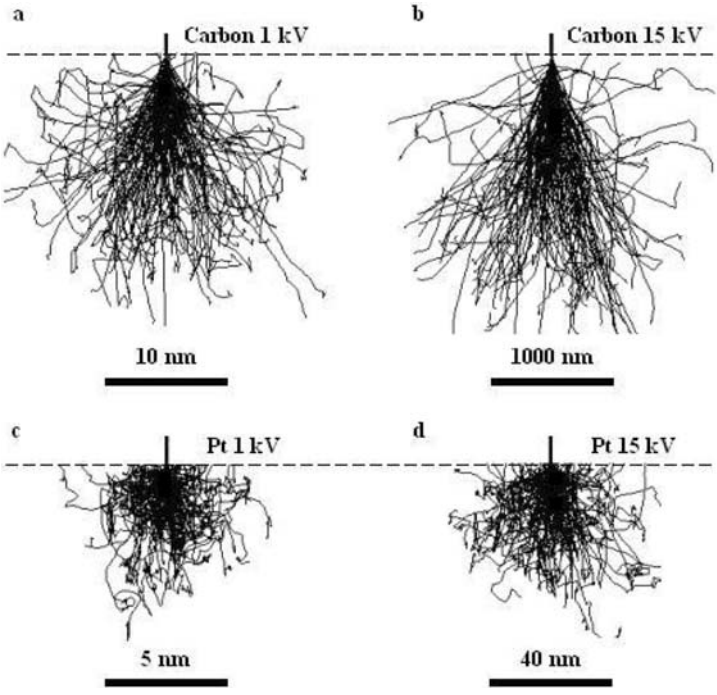

Figure 3. Monte Carlo simulations of the electron beam interactions with bulk carbon (a, b) and platinum (c, d) for 1-keV (a, c) and 15-keV (b, d) electrons, respectively.

low energy electron microscopy (LEEM) may be applicable here if clean surfaces are examined in ultra-high vacuum SEM [33]. In most practical applications, however, this condition will not be met.

Although the electron backscattering coefficient of a bulk sample is almost constant for electrons with energies >10 keV, it changes significantly between 1 keV and 10 keV because of the stronger electron-specimen interactions at low energies. For incident electrons with energies >10 keV, the electron backscattering coefficient increases monotonically with increasing Z. At low energies, however, with decreasing electron energy the electron backscattering coefficient increases for low-Z materials and decreases for high-Z materials. Therefore, we have to be cautious in interpreting low-voltage backscattered electron images. At ultra-low voltages, both the SE and BE signals are surface sensitive and it is possible that the BE signal may have an average escape depth smaller than that of the corresponding SE signal. Strongest surface interactions occur for electrons with energies in the range of 20 eV to 100 eV.

The drastic reduction in the interaction volume provides many advantages of using low-energy electron beam techniques to characterize a plethora of materials including semiconductor devices and nanoparticles. With low-energy electrons, we can perform high spatial resolution microanalysis of bulk samples; we can reduce the

electron-induced damaging of delicate specimens; we can tune the surface-sensitivity of the detected signals; and we can examine non-conducting or less conducting materials with high spatial image resolution.

2.2. Electron-Specimen Interactions in Composite Samples

When the sample of interest is chemically non-homogeneous, the electron-specimen interaction processes are more complex. We use here a model system consisting of metallic nanoparticles supported on the surface of, or embedded in, a carbon substrate to illustrate the complexity of electron-specimen interactions in composite systems. The fundamental scattering processes we discussed here should apply to other nanoscale, non-homogeneous systems as well.

To demonstrate the effect of small metal particles on the scattering of incident electrons, we have performed Monte Carlo simulations of the trajectories of incident electrons and the corresponding backscattering coefficients from small particles supported on, or embedded in, a bulk substrate. Backscattered electrons are defined here as those incident electrons that are scattered out of the target after suffering single or multiple deflections through such an angle that they leave the target on the side by which they entered. A plural scattering model with appropriate modified scattering cross-sections was used for all the simulations [32].

Figures 4a and 4b show electron trajectories in bulk carbon for electron energies of 3 keV and 30 keV, respectively. In the plots shown in Fig. 4, the trajectories of all incident electrons are traced until they rest in the sample or escape out of the sample. It is clearly shown that a large number of the 3-keV electrons are multiply scattered close to the electron entrance surface while the 30-keV electrons penetrate deep inside the carbon without encountering many scattering events. When a small, heavy-element particle is located on, or inside, a light-element substrate, the electron-specimen interaction with the composite sample is more complicated. Depending on the size and the location of the particle as well as the energy of the incident electrons, the electron-particle interaction may play a dominant role in determining the scattering processes of the incident electrons. Figures 4c and 4d show trajectories of 3-keV and 30-keV electrons, respectively, for normal incidence at the center of a Pt particle with a size of 20-nm in diameter, positioned on the external surface of a carbon substrate. Most of the 3-keV electrons interact strongly with the 20-nm Pt particle and a large fraction of the incident electrons can escape at the particle surface as backscattered or as high-angle scattered electrons (The trajectories of the backscattered electrons are not easily discernible in the plot. But careful examination of Figure 4c should show that many of the incident electrons are backscattered by the small Pt particle). In contrast, most of the 30-keV electrons penetrate through the particle and diffuse deep into the carbon substrate although a few of the incident electrons can escape the particle surface. Note that some of the high-angle scattered electrons re-enter the carbon substrate and can travel along the carbon surface for a distance from several to tens of microns. These "grazing" electrons can generate appreciable amount of secondary electrons from the carbon substrate. When the 20-nm Pt particle is positioned 20 nm below the

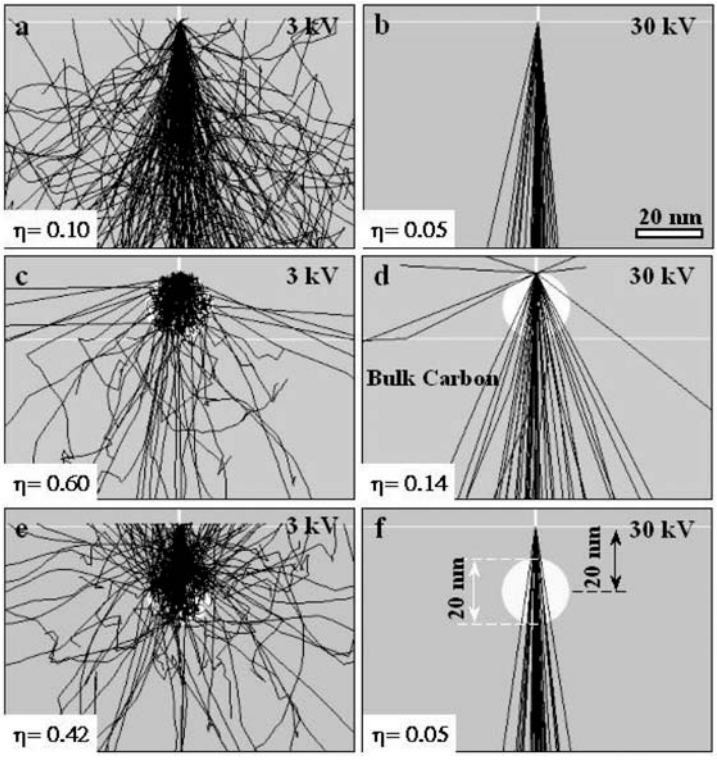

Figure 4. Monte Carlo simulations of the electron beam interactions with bulk carbon (a, b), a 20 nm Pt particle on the surface of the carbon support (c, d), and a 20 nm Pt particle located 20 nm inside the carbon support (e, f) for 3-keV (left hand side) and 30-keV (right hand side) electrons, respectively. The backscattering coefficients are also shown.

carbon surface, a large fraction of the 3-keV electrons are first backscattered by the Pt particle, then travel through the carbon substrate, and finally exit the carbon surface as backscattered electrons (Fig. 4e). The 30-keV electrons, however, do not experience significant high-angle scattering events (Fig. 4f); most of the high-energy electrons pass through the Pt particle without being backscattered.

The value of η for a particle-substrate composite strongly depends on the primary electron energy E and the size and location of the particle. A 20-nm Pt particle located on the surface of a carbon support may give a very high contrast in BE images obtained with 3-keV electrons since $\eta_P = 0.6$ for the platinum-carbon composite sample and $\eta_C = 0.1$ for the carbon support. A contrast

$$C = 100\% \times (\eta_P - \eta_C)/(\eta_P + \eta_C) = 71\% \quad (1)$$

is then obtained for this Pt particle in high-resolution BE images. On the other hand, a 20-nm Pt particle embedded 20 nm below the surface of the carbon support may not be

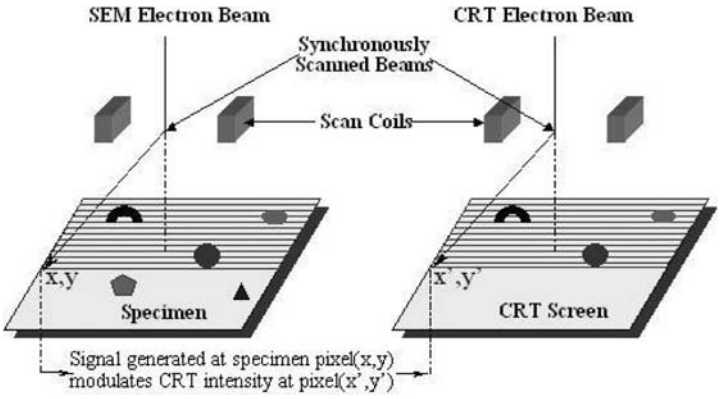

Figure 5. Schematic diagram illustrates the formation of SEM images.

easily observed in BE images obtained with 30-keV electrons (Fig. 4f) since the electron backscattering coefficient for the particle-carbon composite sample ($\eta_P = 0.05$) does not change appreciably from that for pure carbon. If 3-keV electrons are used (Fig. 4e), this Pt particle, however, can be easily observed with a contrast of about 62% since now $\eta_P = 0.42$, much larger than that of pure carbon. Electron interactions with composite samples are complicated, especially when low-energy electrons are used. The interaction processes of low-energy electrons also critically depend on the size of the Pt particle. For example, although 3-keV electrons cannot penetrate through a Pt particle with a size of 50 nm in diameter, electrons scattered to high angles by the Pt particle can exit the particle surface and strongly interact with the carbon substrate.

3. INSTRUMENTATION OF THE SCANNING ELECTRON MICROSCOPE

3.1. General Description

Unlike in a TEM where a stationary, parallel electron beam is used to form images, the SEM, similar to that of a fax machine or a scanning probe microscope, is a mapping device. In a SEM instrument, a fine electron probe, formed by using a strong objective lens to de-magnify a small electron source, is scanned over a specimen in a two-dimensional raster. Signals generated from the specimen are detected, amplified, and used to modulate the brightness of a second electron beam that is scanned synchronously with the SEM electron probe across a cathode-ray-tube (CRT) display. Therefore, a specimen image is mapped onto the CRT display for observation (Fig. 5). If the area scanned on the sample is A_s and the corresponding area on the CRT display is A_d, then the magnification (M) of a SEM image is simply given by $M = A_d/A_s$. The SEM magnification is purely geometric in origin and can be easily changed by varying the scanned area on the sample. These operating principles are the same as those of the STEM instrument.

Since SEM is a serial recording instead of a parallel recording system, the whole process of generating a SEM image could be slower than that in the TEM. A high-quality SEM image usually builds up over several seconds to several minutes, depending on the types of signals; thus, high probe-current within a small electron nanoprobe is desirable and microscope and sample stability is critical to obtaining high-quality and high-resolution SEM images. Unlike in TEM, there is no rotation between the object and image planes, and the microscope magnification can be changed without refocusing the electron beam to obtain an optimum focused image. The resolution of SEM images at high magnifications is primarily determined by the size of the incident electron probe, the stability of the microscope and the sample, and the inherent properties of the signal-generation processes.

Multiple imaging and analytical detectors have been developed to simultaneously collect several signals that can be displayed individually or combined in perfect register with each other. This unique capability makes the SEM a powerful microanalytical tool since multiple views of a sample, in different imaging, diffraction, or spectroscopy modes, can be collected, analyzed, and compared in a single pass of the incident electron beam. When a thin specimen is used, both bright-field (BF) and annular dark-field (ADF) detectors can be used to form STEM images [34]; the image formation theory, the contrast mechanisms, and the applications of the STEM are fully discussed by Cowley in this volume. Figure 6 illustrates the available detectors commonly used for collecting imaging and analytical signals in a modern high-resolution FEG-SEM instrument.

Because of the intrinsic nature of a mapping device, the SEM is ideal for digital imaging and for on-line or off-line processing of images, spectra, and EBSP. Signals from several detectors can be digitally acquired either simultaneously or independently; different signals can also be combined together by addition, subtraction, multiplication, or other mathematical manipulations to gain insight about the structure of the sample. These digital images or spectra can be electronically transferred to remote locations through the intranet/internet or the world-wide-web for live image observation or for fast dissemination of vital information.

3.2. Performance of a Scanning Electron Microscope

The performance of an electron microscope is generally defined by its achievable spatial resolution. In the case of the high spatial resolution FEG-SEM the attainable resolution is determined by many parameters including the diameter d of the effective electron probe, the total beam current I_b contained within that probe, the magnification of the image (or pixel resolution), and the type of the imaging mode and the corresponding electron-specimen interaction processes.

The diameter of the effective electron-probe at the specimen surface is by far the most important parameter that determines the performance of the FEG-SEM. The current distribution in an electron nanoprobe depends on the beam parameters (brightness β, energy E, and energy-spread ΔE), the lens system parameters (spherical and chromatic aberration coefficients C_s and C_c), the application settings (probe current I_b and the aperture angle α), and the focus value f [30].

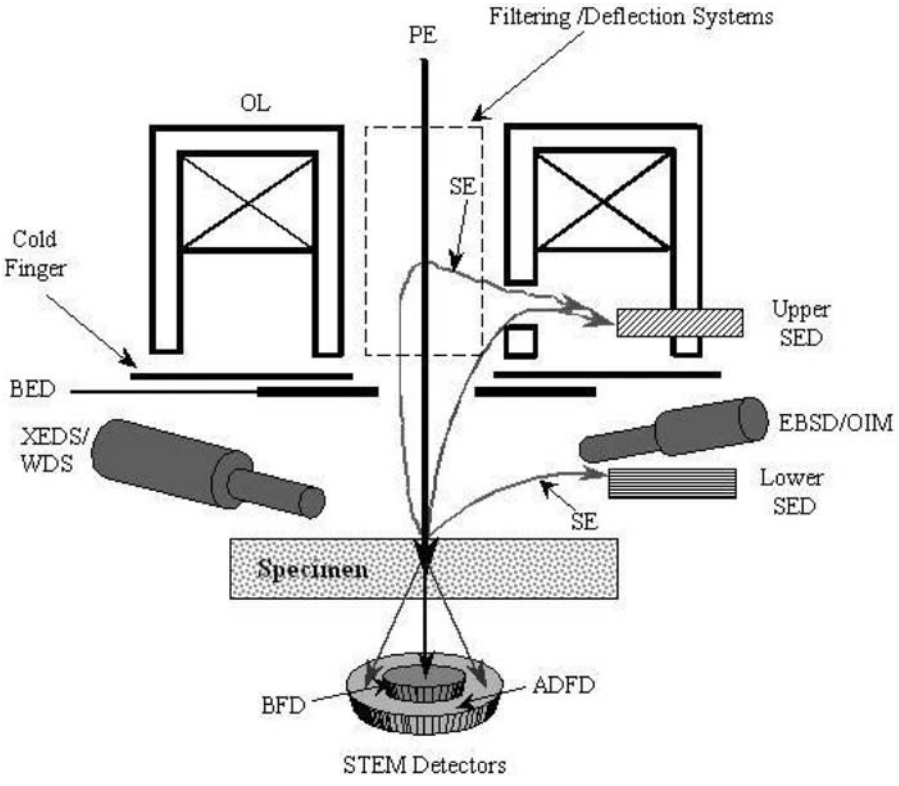

Figure 6. Schematic diagram illustrates the available detectors in a modern FEG-SEM: primary electron (PE), objective lens (OL), secondary electron detector (SED), backscattered electron detector (BED), X-ray energy dispersive spectrometer (XEDS), wavelength dispersive spectrometer (WDS), electron backscattering diffraction (EBSD), orientation imaging microscopy (OIM), secondary electron (SE), bright-field detector (BFD), annular dark-field detector (ADFD), scanning transmission electron microscopy (STEM).

The current density within an electron nanoprobe is not uniform; thus, measurement of the width of the current density distribution is not a good measure of the characteristics of the nanoprobe. The commonly used FWHM (full width at half maximum) method is too simplistic and can give misleading information about the characteristics of the electron probe; electron probes having the same FWHM value can have drastically different current density distributions as shown in Fig. 7 of three very different probes but they all have the same FWHM value. More than 98% of the electrons are contained within the FWHM of the top-hat probe (#1); about 78% of all electrons are contained within the FWHM of the Gaussian probe (#2); and only about 57% of the total number of electrons are contained within the FWHM of the spike probe (#3). Probe #3 may yield higher image resolution but probe #1 can provide a better "analytical" resolution.

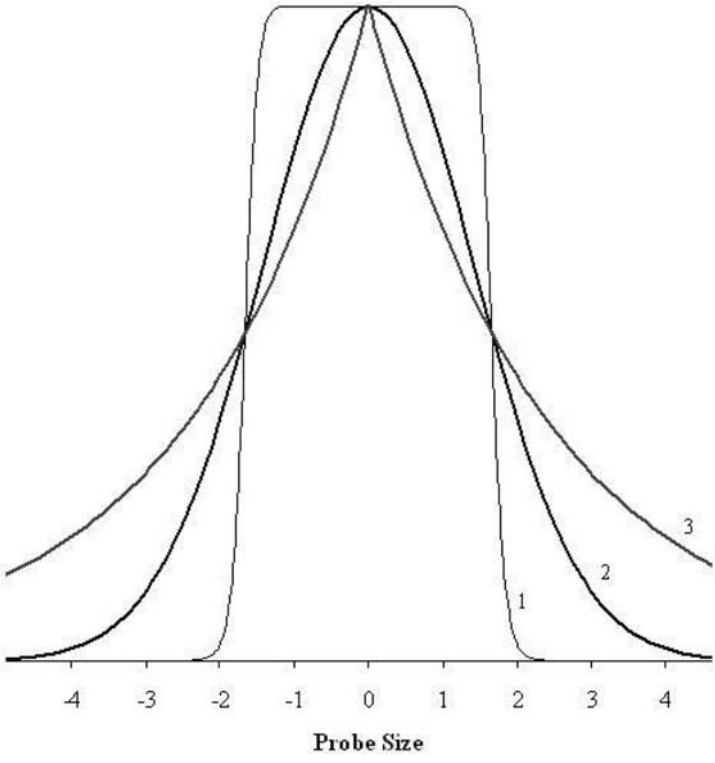

Figure 7. Calculated one-dimensional curves illustrate that different current density distributions within a probe can give the same value of full width at half maximum (FWHM) but may give very different image resolution or contrast.

To most of the practitioners, the full wave optical description of the current density distributions of electron nanoprobes and how these distributions vary with the beam and lens parameters is too complicated to provide intuitive guidance for understanding the electron probe-forming system in a FEG-SEM. Although the probe current distribution in an electron nanoprobe needs to be calculated from the wave-optical theory, geometrical optical theory of the electron-probe formation processes can provide some insights and can provide practical guides to control and to manipulate attainable sizes of the electron nanoprobes.

Considering the geometric probe-diameter d_0 and its broadening due to the action of the lens aberrations of the objective lens, the effective electron-probe diameter d_p can be estimated by [30, 30–36]

$$d_p = \left(d_0^2 + d_d^2 + d_s^2 + d_c^2\right)^{1/2} = \left\{\left[C_0^2 + (0.6\lambda)^2\right]\alpha_p^{-2} + 0.25C_s^2\alpha_p^6 + \left(C_c\frac{\Delta E}{E}\right)^2\alpha_p^2\right\}^{1/2} \quad (2)$$

where d_d is the probe broadening due to the diffraction effect, d_s due to the effect of spherical aberration, and d_c due to the effect of chromatic aberration. The parameter α_p is the electron probe aperture and is defined by the size of the objective aperture. The parameters C_s and C_c are the spherical and chromatic coefficients of the final probe-forming lens, respectively. The parameters λ and E are the wavelength and the energy of the primary electrons, respectively; and ΔE is the energy spread of the electron beam. The parameter C_0 contains the probe current I_p and the gun brightness β and is given by

$$C_0 = \left(\frac{4I_p}{\pi^2\beta}\right)^{1/2} \tag{3}$$

The final probe size is therefore determined by the size of the objective aperture, the gun brightness and the total probe current, the spherical and chromatic aberration coefficients, and the energy and energy spread of the primary electron beam.

Figure 8a shows each of the various factors affecting the effective probe size and their dependence on the probe-aperture angle for two electron energies. The logarithmic plot is used here to show the various dependencies and for easy discussion and visualization. The diffraction lines for both the 30-keV and the 1-keV plots have a slope of -1; the probe size can never reach the regions below these lines due to the uncertainty principle. The plots for chromatic aberration give a line of slope $+1$; the effect of chromatic aberration on the final probe size becomes dominant with decreasing incident electron energy. The effect of spherical aberration does not depend on the incident electron energy; with a line of slope $+3$, it quickly becomes, however, dominant when larger probe apertures are used.

In a modern FEG-SEM, when high-energy electrons (10–30 keV range) are used, the contribution of d_c to the final probe size is negligible; with a high-brightness FEG, the probe size of a high-energy electron beam is primarily determined by the C_s value, the diffraction limit, and the total beam current. When low-energy electrons (<5 keV) are used, however, the effect of the chromatic aberration becomes increasingly dominant and the achievable resolution is primarily limited by the C_c value.

Figure 8a also shows the dependence of the effective probe sizes $d_{1\text{keV}}$ and $d_{30\text{keV}}$ on the probe-aperture angle (ref equation (2)). There exists an optimum probe aperture which provides the minimum probe size. The value of the optimum probe aperture depends on the values of C_c, C_s, C_0, ΔE, and the incident beam energy E. Figure 8b shows the dependence of the minimum probe size on the energy of the incident electrons (RMS curve); and Fig. 8c shows, for 30-keV electrons, how the total probe current affects the obtainable minimum probe size and the value of the optimum probe aperture.

Figure 8d shows how the optimum probe aperture and minimum probe size vary with C_c and C_s values for 1-keV electrons. To achieve a 1-nm probe size with 1-keV electrons both the chromatic and spherical aberrations of the objective lens have to be

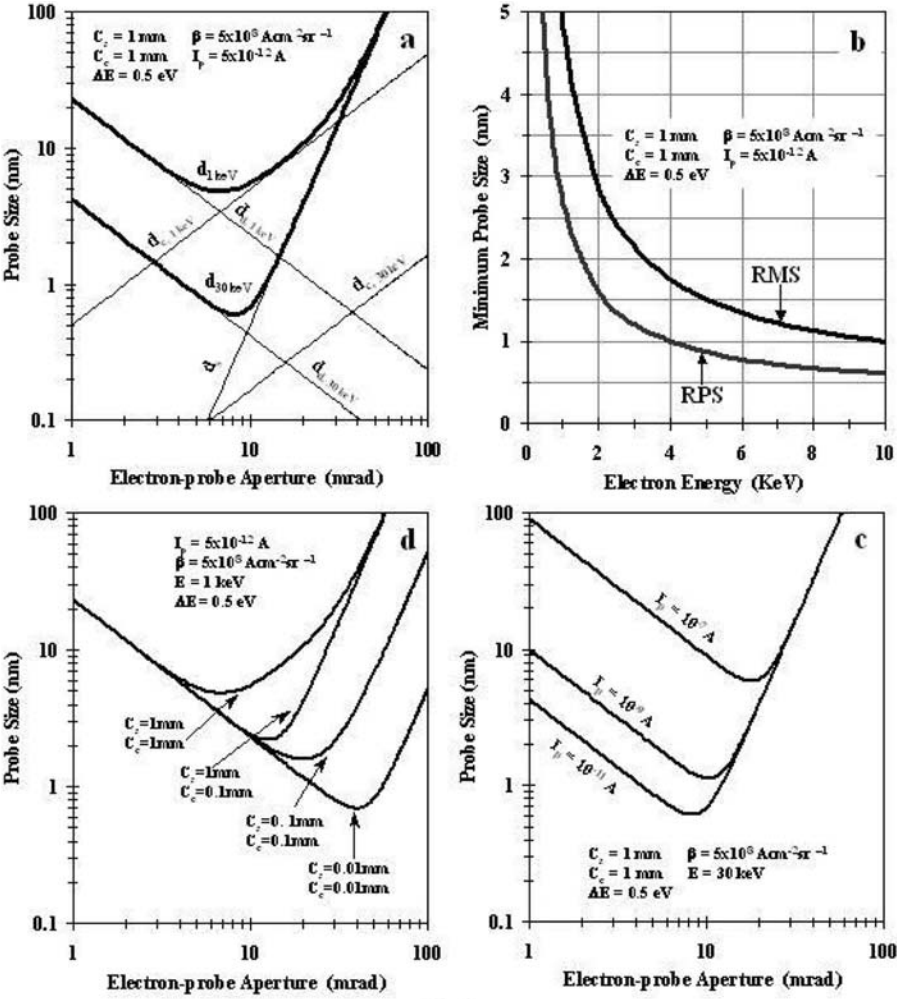

Figure 8. Plots (a) show the dependence of the probe size on the probe-aperture angle for diffraction-limited probe, spherical aberration limited probe, chromatic aberration limited probe, and the root mean square sum of these contributions for 1-keV and 30-keV electrons, respectively. Plots (b) show the dependence of minimum probe size on the primary electron energy based on the root mean square (RMS) rule and the root power sum (RPS) rule. Plots show (c) the dependence of the probe size on the probe-aperture angle for different total beam current values. Plots (d) show the dependence of the obtainable minimum probe sizes on the spherical and chromatic aberration coefficients.

dramatically reduced. This has been recently achieved by using C_c and C_s correctors in a low voltage FEG-SEM [39]. Besides achieving ultrahigh image resolution, other advantages of using aberration-correctors include increase of the total beam current at a given probe size and the increase of the effective working distance without sacrificing the image resolution. For ultra-low-energy electrons, the use of a cathode lens in

combination with the electron-focusing lens may be a better alternative for achieving high spatial resolution imaging [40].

While the plots in Fig. 8 allow us to gain some insight into the various contributions to the probe size formation and how the electron probe changes with the probe aperture, they do not allow us to calculate the smallest probe size achievable. The reason, as pointed out in [37], is that we cannot simply form the root mean square of the various contributions to find the minimum size of the electron probe since different components have very different characters and may not even occur at the same position along the optical axis of the electron microscope. A root-power-sum algorithm is recently proposed to find the optimized probe size for given parameters [38]; and the authors showed that the values obtained from this new algorithm is very close to those given by the full wave optical calculations. The dependence of the optimum probe size (the probe size here is defined as the width of the probe current distribution that contains 50% of the total probe current) calculated from the root-power-sum algorithm is plotted in Fig. 8b (the RPS curve). It clearly shows that the obtainable minimum probe sizes are much smaller than those estimated from equation (2), especially at low energies; the trend, however, is similar.

When high-current electron probes are desired, for example, for applications in electron beam nanolithography, electrons within the finite-sized nanoprobe interact with each other through Coulomb force; the electron-electron repulsive interaction can perturb the axial (along the electron optic axis) and transverse velocities of the emitted electrons, especially at crossovers of intense electron beams. The electron-electron interactions can affect the property of an electron beam in three ways [41]: 1) the space charge effect, 2) the trajectory displacement effect, and 3) the energy broadening effect. The space charge effect refers to the deflection of an electron, traveling along the optic axis, by the effective average charge of all other electrons within the electron beam; the degree of deflection is proportional to the distance of the electron from the optic axis, thus causing a defocus of the electron beam. The space charge effect increases linearly with the total current of the electron beam; it becomes dominant in high current applications.

The effect of defocus on the probe size is a simple first order effect originating from a shift along the optic axis by an amount, say, Δz; this will produce a uniformly illuminated circle of diameter given by $\Delta d = \Delta z \tan \alpha_p$, where α_p is the probe-aperture angle. The effect of defocus on the probe size determines the depth of focus in SEM images. If we assume the resolution on a cathode ray tube display is δ_{CRT}, then the corresponding resolution required at the specimen is given by $\delta = \delta_{CRT}/M$ and specimen details at a depth

$$T = \frac{\delta}{\tan \alpha_p} = \frac{\delta_{CRT}}{M \tan \alpha_p} \tag{4}$$

will appear sharp in the SEM images. If we further define a field width of the image on the CRT display as W_{CRT}, then the width of the scanned area at the specimen is

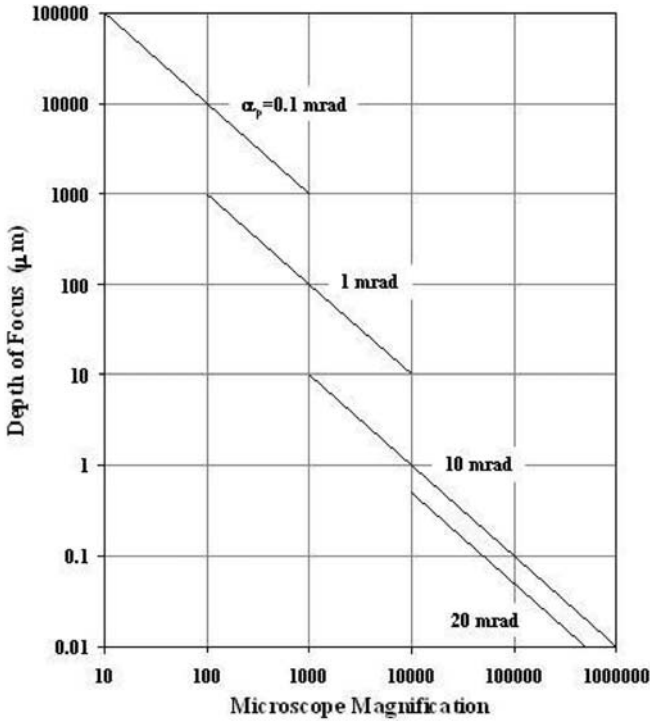

Figure 9. Plots show the dependence of the depth of field in a SE image on the image magnification and the probe-aperture angle. Higher image resolution, which requires larger probe-aperture angles, results in lower depth of field.

given by $W = W_{CRT}/M$. The normalized depth of field t, which is more meaningful in practice, is given by

$$t = \frac{T}{W} = \frac{\delta_{CRT}}{W_{CRT} \tan \alpha_p} \sim \frac{10^{-3}}{\tan \alpha_p} \tag{5}$$

In equation (5), we approximated δ_{CRT} to one pixel and W_{CRT} to 1024 pixels. The normalized depth of focus clearly drops dramatically with the increase of the probe-aperture angle. Figure 9 shows plots of the dependence of depth of focus on the microscope magnification and the probe-aperture angles. In practical applications of a modern FEG-SEM, one needs to effectively utilize the interrelated relationships among probe-aperture angle, magnification, depth of focus, and image resolution.

Figure 8d shows that probe-aperture angles >20 mrad have to be used to obtain a probe size ≤1 nm with low-energy electrons; then, the depth of field in the high-resolution SEM image is only about 5% of the viewing screen. The use of large

probe-aperture angles significantly reduces the depth of focus in SEM images; and thus makes it possible to observe only those features that are located on the focal plane; out of focus features will be highly blurred and contribute only to the image background. This feature can be effectively utilized to obtain confocal SEM images that provide not only high spatial resolution in the x-y plane but also useful information on the z-axis direction. Three-dimensional images of non-flat surfaces may be obtainable with high spatial resolution confocal SEM images.

To effectively employ the power of a modern high-resolution FEG-SEM, the environmental conditions of the microscope become a critical issue. For example, presence of the stray magnetic field near the microscope can severely interfere its performance, especially at low electron energies. Thermal disturbances, mechanical vibrations, and acoustic disturbances can all profoundly affect the performance of a modern-day low voltage SEM.

4. THE RESOLUTION OF SECONDARY AND BACKSCATTERED ELECTRON IMAGES

Probe size and resolution are interrelated in the SEM but they are not the same. The image resolution can be worse but not better than the probe size of the electron beam (Digital processing, via deconvolution processes, may provide a resolution better than the probe size; but these computationally labor-extensive processes are not routinely used for two-dimensional images and deconvolution procedures have their intrinsic limitations.) At low magnifications, the image resolution is usually determined by the pixel size since features smaller than the pixel size cannot be observed. At high magnifications, however, the pixel size may be much smaller than the probe size so resolvable features can be displayed in several pixels. The information source, which we will discuss below, becomes the resolution-limiting factor at high magnifications.

When a SEM image is formed, the specimen is illuminated by a primary beam of a total current I_p with a current density distribution function $i(\boldsymbol{r})$. Upon entering the specimen, the electron probe interacts with a thin slice of material from which various signals can be generated and some of these signals escape from the specimen surface. If we assume that for a point source the spatial distribution of the generated signals can be described by a function $S(\boldsymbol{r})$, then the information source generated by a finite-sized electron probe at position $\boldsymbol{r}$ is given by

$$\int i(\mathbf{r}')\, S(\mathbf{r} - \mathbf{r}')\, \mathrm{d}\mathbf{r}' \tag{6}$$

When a primary electron beam interacts with a specimen, secondary, Auger, and backscattered electrons can all be generated. On their way traveling to the specimen surface, these electrons will generate more secondary electrons with lower energies; therefore, a cascade process occurs within the specimen. If we designate the yield of the secondary electrons that are directly generated by the primary beam as δ, the BE yield as η, and the yield of the secondary electrons that are generated by the

backscattered electrons as $\beta\delta$, then for each probe position the amplitude distribution of the information source in the specimen surface plane is given by

$$\frac{I(\boldsymbol{r})}{I_p} = \delta\int i(\boldsymbol{r}')\,S_\delta(\boldsymbol{r}-\boldsymbol{r}')\mathrm{d}\boldsymbol{r}' + \eta\int i(\boldsymbol{r}')\,S_\eta(\boldsymbol{r}-\boldsymbol{r}')\mathrm{d}\boldsymbol{r}' + \eta\beta\delta\int i(\boldsymbol{r}')\,S_{\eta\delta}(\boldsymbol{r}-\boldsymbol{r}')\mathrm{d}\boldsymbol{r}' \qquad (7)$$

The first term in equation (7) represents the spatial distribution of the secondary electrons that are directly generated by the primary electrons; these secondary electrons are usually called SE1. The second term in equation (7) represents the spatial distribution of the backscattered electrons at the specimen surface. The third term in equation (7) represents the spatial distribution of the secondary electrons that are generated by the backscattered electrons; these secondary electrons are usually called SE2.

Detailed calculations of equation (7) is not possible at the present time since the $S(r)$ functions are not known although many approximations and models have been proposed to gain insights into the generation, diffusion, and escape processes of the backscattered and secondary electrons. Monte Carlo simulations, however, have provided useful knowledge on the electron-specimen interaction and SE generation processes (see reference [42] for a recent review). When high-energy electrons are employed, the SE1 and SE2 can be spatially separated since the SE1 signal is localized within a very close range of the impact position of the incident electron beam, but the SE2 signal can originate from a region similar to that of the electron range of the primary electron beam. Although the strength of the SE2 signal can be higher than that of the SE1 due to the cascading process, the current density distribution of the SE1 signal is much more shaper than that of the SE2 signal. Therefore, at high magnifications, the resolution of the SE image is determined by the spatial distribution of the SE1 signal; the SE2 signal contributes to the background of the high magnification SE images. Since the strength of the SE1 signal may be only a small fraction of that of the SE2 signal, the high-resolution details revealed in a SE image has poor signal-to-noise and signal-to-background ratios.

At middle range magnifications, the pixel size may be close to the range of the SE2 signal and the image resolution and contrast are now determined by the properties of the SE2 since SE2 contributes to most of the detected signal. We should note that the energy distribution of the SE1 signal could not be distinguished from that of the SE2 signal. Only if a very thin specimen is used can SE2 be significantly reduced or eliminated. The SE2 signal should carry information similar to that of the BE signal.

When the energy of the primary electron probe is reduced, the range of the SE2 signal significantly decreases as demonstrated in Figure 3. The spatial distribution of the SE2 approaches that of the SE1 signal; thus, the SE1 and SE2 signals can no longer be differentiated even at high magnifications. In this case, both components contribute to high-resolution information; thus, high-resolution SEM is significantly more efficient at low electron energies although the probe size may be larger as demonstrated in Fig. 8. With the use of aberration correctors, the resolution of an SEM will become less dependent on the primary beam energy; the accelerating voltage of the SEM can

therefore be used to modulate the interaction volume, to optimize the image contrast, or to probe the subsurface information.

The ultimate resolution limit of SE imaging is determined by the first term in equation (7). When a point probe or a very small electron probe is used, the image resolution is determined by the source function $S_\delta(r)$. The ultimate resolution is determined by the spatial distribution of the secondary electrons initially excited by the primary beam; the subsequent transportation of these hot electrons toward the specimen surface may not deteriorate the image resolution. The values of the inelastic mean free paths of the generated secondary electrons are not related to the ultimate achievable resolution of SE images at all; very high-resolution SE images of insulators such as MgO smoke crystals have been obtained [43].

To determine the source function $S_\delta(r)$ we need to know the specific processes for generating secondary electrons inside solid specimens; this is a non-trivial problem and the detailed discussions are beyond the scope of this chapter. Recent data from the electron coincidence spectroscopy experiments [44–45] confirmed the early proposal that the high-resolution SE signals are generated via large momentum transfer excitation events and are thus highly localized in the initial generation process [15]. The detailed generation and escape processes of SE1 signals are still not clearly understood. Inner-shell and single electron valence excitations may account for the SE production, especially for the high spatial resolution signals [46].

The resolution and the contrast of a SE image depend on the rate at which the collected signal changes as the electron probe is moved across a non-homogeneous region; and this depends primarily on the change in the number of the collected signals. Thus, even if the escape distance is not very small and the acquired signals actually originate from some other region of the specimen, variations in composition, for example, can still be detected over small distances because of the associated change in the elastic or inelastic scattering events of the primary electrons.

In view of the above discussion, BE signals can also provide high spatial resolution information; and the high sensitivity of the BE signal to the atomic number Z of solid materials makes the high-resolution BE imaging the method of choice in the modern FEG-SEM for providing compositional information on a nanometer scale. Nanometer-scale metal nanoparticles in supported catalysts can be easily detected by collecting the BE signal; information on the spatial and size distributions of metal nanoparticles can be obtained on bulk samples and even the depth distribution of the metal nanoparticles can be inferred [20]. At lower primary beam energies, the BE signal becomes more surface sensitive and its source of generation becomes much smaller, approaching that of the SE1. The recent development of high-sensitivity BE detectors will make the BE imaging or the combination of BE and SE imaging the most powerful tool for studying nanophase materials or other nanosystems.

The current achievable image resolution in a modern FEG-SEM is still primarily limited by the achievable probe size and poor signal-to-noise ratio. An image resolution of about 0.5 nm or better, however, can be achieved in both the in-lens type FEG-SEM or in STEM instruments. Atomic resolution imaging, for example, of lattice

fringes of bulk crystals that are oriented at the exact channeling conditions, has not been achieved yet.

5. CONTRAST MECHANISMS OF SE AND BE IMAGES OF NANOPARTICLES AND OTHER SYSTEMS

The contrast mechanisms of SE images have been of extensive study ever since the SEM was invented. Depending on the materials of interest many factors can contribute to the observed image contrast: material contrast, topographic contrast, voltage contrast, magnetic contrast, electron channeling contrast, charging contrast, etc. Some or most of these contrast mechanisms may play a role in the SE images of interest. Detailed discussions on the origin of these contrast mechanisms have been well documented in literature and readers of interest should consult the relevant textbooks, for example, references [30–31]. We will briefly discuss below, however, some recent developments that are relevant to the study of nanosystems and surfaces.

5.1. Small Particle Contrast in High-Resolution BE Images

The small particle contrast is of interest to correctly interpreting high-resolution SE and BE images of supported catalysts, nanoparticle systems, or other nanoscale systems. Figure 10 shows a set of SE and BE images of a carbon supported Pt catalyst obtained with different primary electron energies; all the images were obtained from the same sample region. Because of its high Z-contrast, the high-resolution BE images clearly revealed the Pt nanoparticles located either on the carbon surface or within the highly porous carbon support. A better image resolution is achieved at higher incident electron energies because of the smaller size of the incident probe and less beam broadening in the sample. The image intensity of a Pt nanoparticle does not necessarily increase monotonically with its size in BE images.

In Fig. 10a, for example, some smaller Pt particles (e.g., the particle indicated by the letter B) clearly have higher visibility than that of some bigger Pt particles (e.g., the Pt particle indicated by the letter A). In Fig. 10b, however, the particle A shows a much higher intensity than that of particle B. The interpretation of high-resolution BE images of supported nanoparticles is complicated and many factors may contribute to the observed image contrast. To understand the effect of the incident electron energy and the size and location of Pt nanoparticles on the particle contrast, Fig. 11a shows the dependence of $\eta(E)$ on incident electron energy for various sizes of Pt particles located on the surface of a bulk carbon support. The values of $\eta(E)$ for bulk carbon and bulk Pt are also shown for comparison. With increasing electron energy, $\eta(E)$ first increases, reaches a maximum, and then slowly decreases. This trend is true for all sizes of the particles although the rate of change depends on the particle size. For each particle size, there exists an optimum electron energy, E_{op}, which gives a maximum value of $\eta_{max}(E_{op})$. This maximum value is reached when the range ($R(E_{op})$) of the incident electrons is about the diameter d of the Pt particle. The E_{op} value increases with the size of the Pt nanoparticle. Note that the maximum value of the backscattering coefficient η_{max} from a small Pt nanoparticle is about the same for different sizes of particles. The

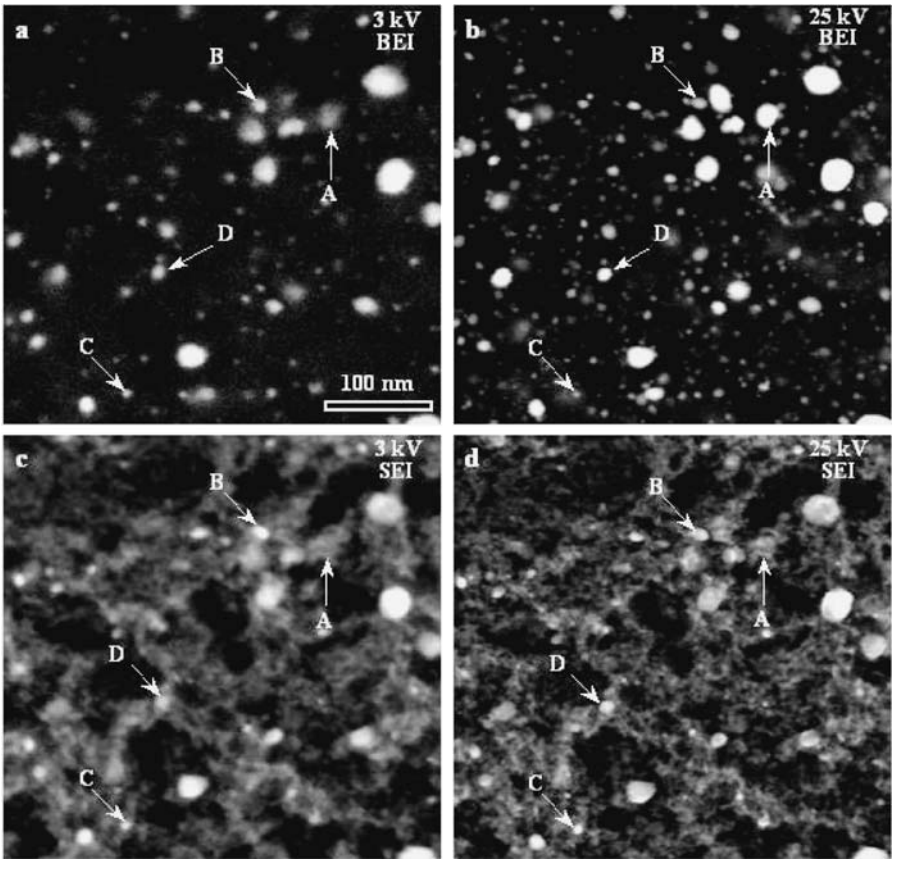

Figure 10. High-resolution SE and BE images of a Pt/C catalyst obtained with the primary electron energies of 3 keV and 20 keV, respectively, clearly showing the spatial and size distribution of the Pt nanoparticles as well as the detailed morphology of the carbon support. See text for detailed discussion.

value of η_{max} may be related to the scaling parameter $\alpha = d/R(E_{op})$ which is about unity for all particle sizes. For smaller Pt particles, although η decreases rapidly with increasing electron energy it does not approach the value of bulk carbon. Thus, small Pt particles positioned on the surface of a carbon substrate will always give an observable bright contrast in high-resolution BE images regardless of the incident electron energy.

Figure 11b shows the dependence of $\eta(d)$ on the size of a Pt particle at different electron energies. With low-energy electrons, a smaller Pt particle may have a higher intensity at the center of the particle than that of a larger Pt particle. For example, a 20 nm Pt particle will give a maximum contrast in BE images obtained with 4 keV electrons while both smaller and larger particles will give a lower image contrast. With

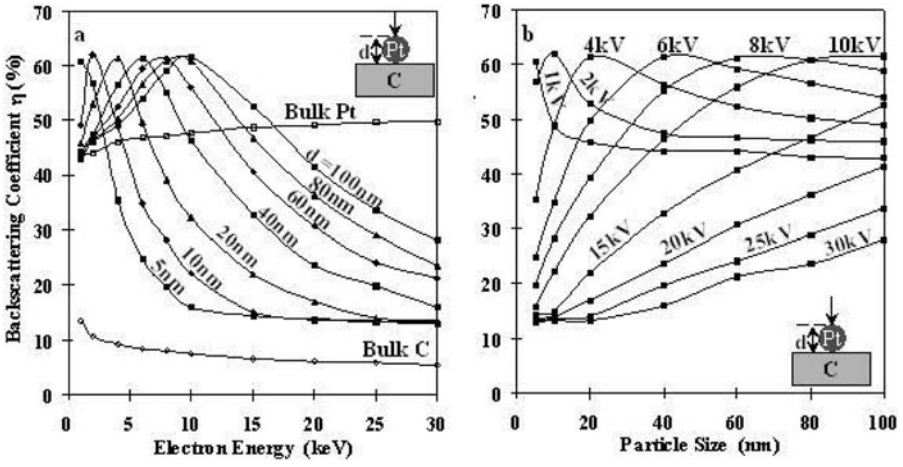

Figure 11. Monte Carlo calculations of backscattering coefficients (η) of Pt particles positioned on a carbon substrate: (a) as a function of electron energy for various sizes of Pt particles and (b) as a function of the size of Pt particles for various energies of the incident electrons. The values of η for bulk carbon and bulk platinum are also shown for comparison. Number of trajectories used: 30,000.

higher-energy electrons, however, the image intensity of a small Pt particle increases monotonically with its size. With further increases of the particle size, the η values for all electron energies will gradually approach their corresponding values of bulk Pt. Figure 11 indicates that the interpretation of high-voltage BE images of small Pt particles located on the surface of bulk substrates is straight forward while that of low-voltage BE images is more complicated.

Another complicating factor in interpreting BE images of supported metal catalysts or other inhomogeneous systems is that some small particles are often located below the substrate surface. For example, some of the small Pt particles with a diffuse contrast in Fig. 10a (e.g., particle A) are definitely located at various depths below the carbon surface. Monte Carlo simulations of the contrast of nanoparticles embedded within matrix materials have been performed [20]. Regardless of the incident electron energy, the backscattering coefficient is the highest when the Pt particle is located on the surface of the carbon substrate. The backscattering coefficient or the contrast of BE images, however, is sensitive to the geometry of the particle-matrix composite as well as the location of the nanoparticle. When a nanoparticle is located below the substrate surface, the incident electrons are first scattered by a layer of the substrate material and then are scattered by the nanoparticle. The electrons backscattered by the nanoparticle will be scattered again by a layer of carbon before they can finally exit the substrate surface as backscattered electrons. Since the energy of the incident electrons is continuously decreasing during these scattering processes and the electron backscattering coefficients from small nanoparticles strongly depend on the energy of the electrons (see Fig. 11a) the electron backscattering processes from

the particle-matrix composite can be very complex. The particle-substrate interface may also play an important role in contributing to high-angle scattering events.

The Monte Carlo calculations clearly show the complex nature of the contrast of small Pt particles in high-resolution BE images of carbon supported Pt catalysts, especially at low voltages. However, by examining high-resolution BE images obtained with different incident electron energies and by comparing these BE images with the corresponding SE images, information about the lateral distribution as well as the depth distribution of metal nanoparticles in supported metal catalysts can be extracted [20].

5.2. Small Particle Contrast in High-Resolution SE Images

High-resolution SE imaging of supported metal catalyst samples was first demonstrated with 100-keV electrons in the STEM [13, 47–48]. The increased emission of secondary electrons from small, heavy-element particles is partially attributed to the local increase in the stopping power of high-energy electrons. Topographical contrast is also a main factor that contributes to the observed bright contrast of small particles. With high-energy incident electrons, the integrated SE intensity of a small metal particle is proportional to the total number of atoms within that particle [49], suggesting that the number of secondary electrons generated is proportional to the total stopping power of a small particle. Small metal particles embedded inside supporting materials may not be revealed in high-resolution SE images [43]. Only those metal particles that lay on, or very close to, the sample surface can give observable image contrast.

When the energy of the incident electrons decreases from high energies, the electron backscattering from a small, heavy-element particle increases. The backscattered electrons generate additional secondary electrons when they pass through the specimen surface (SE2 signal) or when they impinge onto the pole pieces and other parts of the optical system and specimen chamber (SE3 signal). Both the SE2 and SE3 signals carry information similar to that of backscattered electrons. Therefore, if the SE2 and SE3 signals significantly contribute to the collected SE signal then metal particles located deep inside a light-element support may also be revealed in high-resolution SE images.

To understand the contrast of small Pt particles in high-resolution SE images, both the BE and SE signals were collected to form images of the same area of a Pt/carbon catalyst (see Fig. 10). The relatively poorer image resolution shown in Fig. 10a and 10c is partially attributed to the larger working distance (WD = 7 mm) used to accommodate the retractable BE detector. The visibility of the smaller Pt particles in SE images is clearly low when compared to that in the corresponding BE images. Furthermore, only some of the Pt particles which are visible in the BE images are revealed in the SE images. Because of the deeper penetration of electrons at higher energies, more Pt particles are revealed in the higher energy BE image. In contrast, Fig. 10d shows almost the same number of Pt particles, with an improvement in image resolution though, as those revealed in Fig. 10c. Some smaller Pt particles (e.g., the particle indicated by the letter C) have a surprisingly high contrast compared to that of some bigger particles (e.g., the particle indicated by the letter D). While some Pt

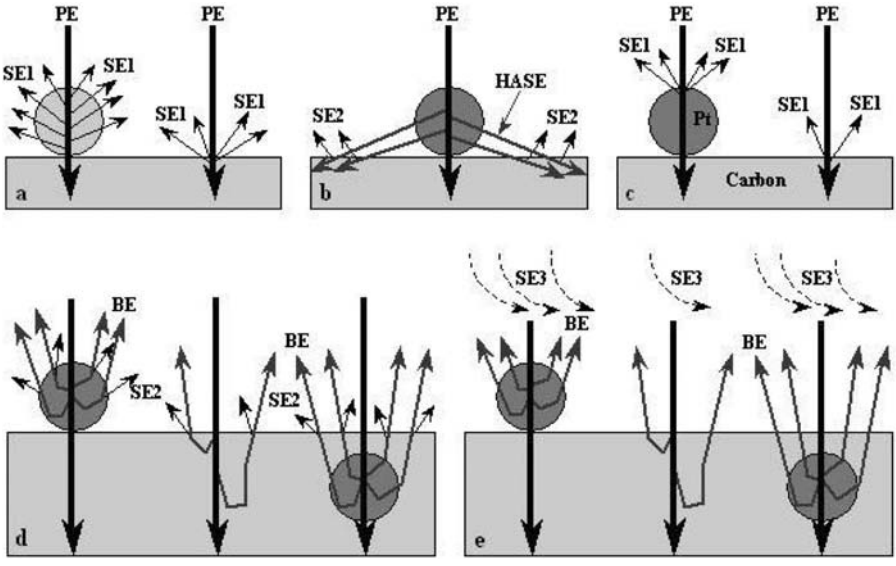

Figure 12. Schematic diagrams illustrate the contributions of various SE signals to the small-particle contrast in high-resolution SE images. PE—primary electrons; SE1—type 1 secondary electrons; SE2—type 2 secondary electrons; SE3—type 3 secondary electrons; HASE—high-angle scattered electrons; BE—backscattered electrons.

particles (e.g., the particle indicated by the letter B) are clearly visible in both the BE and SE images other Pt particles (e.g., the particle indicated by the letter A) are only revealed in the BE images. If we assume that the particle A was embedded inside the carbon support then the variations of the visibility of the particle A in both the BE and SE images of different primary electron energies can be explained. The visibility of small Pt particles in the SE images is also affected by the dominating topographic contrast of the carbon mesopores. A small positive voltage applied to the specimen can, however, greatly suppress the topographic contrast of the carbon support and thus enhance the visibility of metal nanoparticles [50].

The visibility of small metal particles in high-resolution SE images of supported metal catalysts is determined by the following factors: a) topographic contrast; b) diffusion contrast; c) material contrast due to the SE1 signal; d) material contrast due to the SE2 signal; and e) material contrast due to the SE3 signal. Experimental results showed that only those metal nanoparticles that are located on, or very close to, the surface of the substrate can be observable in high-resolution SE images.

The topographic contrast may play a dominant role for nanoparticles located on the surface of a substrate as illustrated in Fig. 12a. When the radius of a small particle becomes comparable to, or smaller than, the escape depths of the secondary electrons, most of the secondary electrons, generated inside the particle, with energies higher than the surface barrier may escape from the particle. In contrast, because of the

total internal reflection of low-energy secondary electrons only about 10% of the total internal secondary electrons that are generated within the escape depth region, can escape from a flat surface. Because of this geometric effect in SE emission from spherical particles, small particles located on a flat substrate surface, even if the substrate and the particle are the same material, are often observed with a bright contrast in high-resolution SE images. In fact, small particles of low-Z materials supported on high-Z substrates can often give a bright image contrast because of this dominant topographic effect; this is in striking contrast to BE images in which high-Z materials always give bright image contrast.

The topographic contrast of small particles can be delineated by the ratio of the particle radius (R) to the average escape depth (L) of the collected secondary electrons. If $R/L \ll 1$, the image intensity is proportional to the total number of atoms within that particle. If $R/L < 1$, the image intensity increases with the particle size and has a maximum at the center of the particle. If $R/L > 1$, the image intensity slowly increases with particle size and the highest image intensity is approximately located at a distance $d = (R–L)$ from the center of the particle. If $R/L \gg 1$, the particle contrast evolves into the edge-brightness contrast, commonly observed in SE images.

For heavy-element particles located on the surface of a light-element support, electrons scattered to high angles (<90 degrees) by a small particle can re-enter the substrate at a glancing angle as schematically illustrated in figure 12b. Monte Carlo simulations show that these high-angle scattered electrons (HASE) can travel a long distance inside the substrate, generating additional secondary electrons that lie within the escape depth of the substrate material. These "extra" secondary electrons will add to the bright, topographic contrast of small particles. This electron diffusion effect is enhanced at low electron energies as demonstrated by the Monte Carlo simulations shown in Fig. 4. This electron diffusion contrast is significantly reduced for particles located just below the substrate surface. The fraction of high-angle scattered electrons by a small, heavy-element particle depends on the size and shape of the particle, the incident electron energy, the average atomic number of the particle, and the location of the particle relative to the substrate surface.

The increased stopping power in a small particle of heavy-element materials can generate more secondary electrons (SE1) per unit volume than that in the light-element supports (schematically illustrated in Fig. 12c). Taking into consideration of the effects of work function and escape depth on the emission of secondary electrons, heavy-element materials may have a higher SE yield than that of light-element materials. Thus, a material contrast may contribute to the visibility of nanoparticles in SE images. There is, however, no direct correlation between the SE yield of a material and its atomic number. So it cannot be generalized that high-Z elements will have a higher SE yield even though they may have a higher electron stopping power. For example, some non-conducting materials may have a much higher SE yield than that of heavy-element metals.

The SE2 signal due to a small, heavy-element particle can be generated within, and escape from the surface of, a small particle (if the particle is located on the surface of the substrate). They can also be generated in the substrate (if the particle is embedded in

the substrate) and escape from the sample surface (schematically illustrated in Fig. 12d). Because of the higher BE yield from small, heavy-element particles, especially at low electron energies (see Fig. 4), more SE2 signals are generated whenever the incident electrons encounter a small particle. The small-particle contrast due to the SE2 signal is directly related to the image contrast of the corresponding BE images.

Similar to the discussion for the SE2 signal, the SE3 signal also carries information directly related to that of the BE signal (Fig. 12e). The SE3 signal should also give a bright contrast in SE images of small, heavy-element particles. Without special arrangements of the SE detection system, the effects of the SE2 and SE3 signals on the small-particle contrast cannot be distinguished or eliminated. Experimental results showed, however, that the contribution of the SE2 and SE3 signals from small, heavy-element particles to the collected SE signal may not be significant; the contribution of these signals from larger particles, however, may be appreciable [20].

5.3. Other Contrast Mechanisms

The contrast in both SE and BE images is a number contrast; any change (above the statistical noise level) in the number of the collected signal will give an image contrast. Thus, change in work function, which affects the emission step of the internal secondary electrons, can be visualized in biased SE images [51–52]. Submonolayer, monolayer, or multilayer deposits can be readily visualized and distinguished.

By using a directionally sensitive detection system, it is also possible to reveal, in strong contrast, atomic steps and the crystallographically equivalent but differently oriented 1×2 and 2×1 domains at the reconstructed Si (100) surface [53]. The origin of this contrast could come from a Bragg reflection effect in the reconstructed layer with a strong dependence on the azimuthal direction of the electron crossing the surface barrier [46]. Since the energy distribution of the internal secondary electrons near the surface of the specimen is highly skewed toward low energies, any change of the work function or even the shape of the surface potential may intricately modify the SE emission probability, especially when an external field is applied.

Local potential variations on a non-homogeneous specimen surface generate patch fields, which may influence the emission or movement of the secondary electrons. Depending on the polarity of the patch fields, these regions may give a reduced or enhanced SE emission, especially in the low energy part of the SE spectrum. There is not much experimental or theoretical work done on the effect of local patch fields, which may be becoming increasingly important in understanding nanosystems, on the emission of secondary electrons or on the image contrast of high-resolution SE images. Recent interest in this topic [46] may provide much needed impetus for further exploration on the possibility of high-resolution imaging of local variations in work function, contact potential, or even charge transfer in nanoscale systems.

Changes in surface barrier height or subsurface band bending effects have recently been shown to provide good image contrast of p-n junctions in high-resolution images of doped semiconductor devices [54]. The authors observed that the p-type regions always appear brighter relative to the n-type regions in a doped GaAs sample. The

observed contrast was attributed to band pinning effects associated with the chemisorption of oxygen at the sample surface, which enhances the yield variations between the p- and n-type regions; band bending and the modification of the shape of the surface potential may as well play a role in the observed image contrast. The effect of energy filtering by the in-lens type FEG-SEM, which was used to obtain these results, on the observed image contrast was also proposed [21].

6. APPLICATIONS TO CHARACTERIZING NANOPHASE MATERIALS

High-resolution SEM imaging can be conveniently applied to extract nanoscale information from many different types of nanophase materials or systems. Any solid materials, even soft materials, can be imaged in a modern FEG-SEM; with the use of a cryo system or by using an environmental SEM, almost all the organic and inorganic materials can be examined and useful information about the morphology, ultrastructure, and composition of the region of interest can be extracted. Not only nanophase materials but also intact micro- or nano-devices can be imaged in the modern day, large chamber FEG-SEM instruments.

High-resolution SEM imaging and associated techniques are now routinely used in the semiconductor industry for failure analyses of semiconductor devices, for example, analyses of cell-blocks, trench capacitors, bit lines, gate conductors, or cross-sections of the DRAM cells. Specialized electron beam lithography and wafer processing inspection systems have been in extensive use in the semiconductor industry. Critical dimension measurements and nano-metrology will become more critical to the successful development of next generations of micro and nanodevices. Creation of micro electro mechanical systems, nanostructures, and nanodevices is certainly the most important frontier of nanoscience research and nanotechnology. To know what we have created or how they work or how to make improvements, we need to use high-resolution FEG-SEM techniques to examine these devices or materials. It is expected that the high-resolution FEG-SEM will become the most important tool in developing nanotechnology products, especially nanodevices and bio-nanodevices.

As an example of applications, Fig. 13a shows a low voltage (1 KV), high-resolution SE image of a freshly fractured IC device clearly showing the individual components. The cross-section device could not be examined at high voltages due to severe sample charging effect [25]. In this particular case, low-voltage SE imaging proves to be more useful and reliable. High-resolution BE images, especially at low voltages, also provided useful information on the identification and measurement of the individual components. Rapid and reliable identification of defects and high throughput are of essence here.

On the other hand, Fig. 13b shows a high voltage (100 KV), high resolution SE image of a MgO smoke crystal, clearly revealing surface steps, facets, and the various faces of the incomplete MgO cube. Individual (111) planes are not charge neutral; the presence of a net dipole moment normal to the surface leads to a divergence in the surface energy. Therefore, the (111) planes are not stable and facet into (100) planes as clearly shown in Fig. 13b. Figure 13b also shows that the MgO (110) planes are

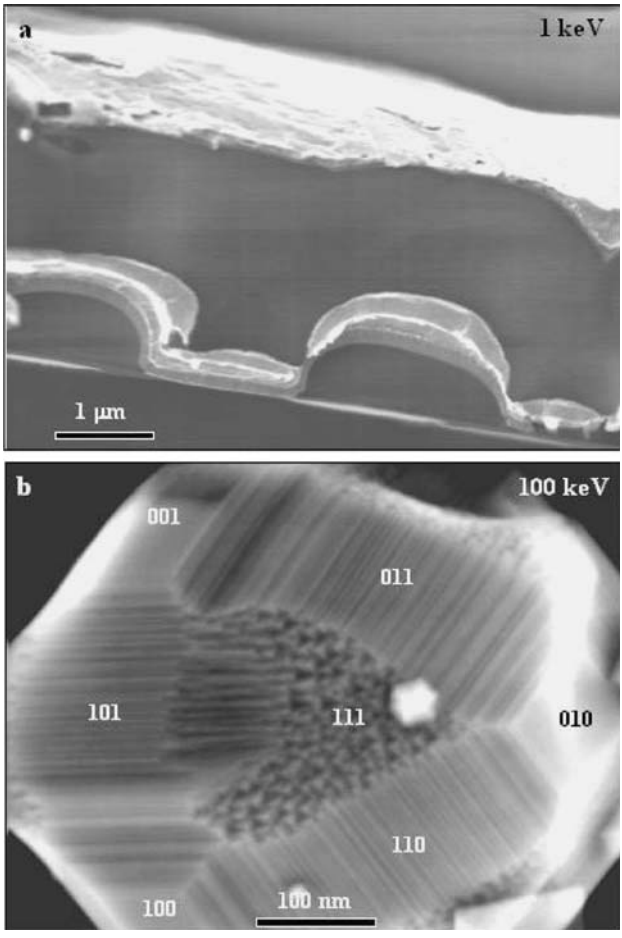

Figure 13. High-resolution, low-voltage SE image of a freshly fractured IC device clearly showing the different components of the device (a); high-resolution, high-voltage SE image of a MgO smoke crystal revealing steps, facets, and the different planes of the incomplete MgO cube (b).

also not stable although these surfaces are non-polar with equal numbers of cations and anions in each atomic plane parallel to the surface. The surface energy of MgO (110), however, is reported to be much higher than that for the (100) surface [55]; thus, the MgO (110) may relax or exhibit rumpling. The high-resolution SE image in Fig. 13b clearly shows that the (110) surfaces of the MgO smoke are not smooth and are faceted toward (100) planes, at least along the direction connecting the different (110) planes. These studies are important for understanding the formation mechanisms of nanoparticles or nanocrystals and for the interactions between metallic nanoparticles and metal oxide nanocrystals.

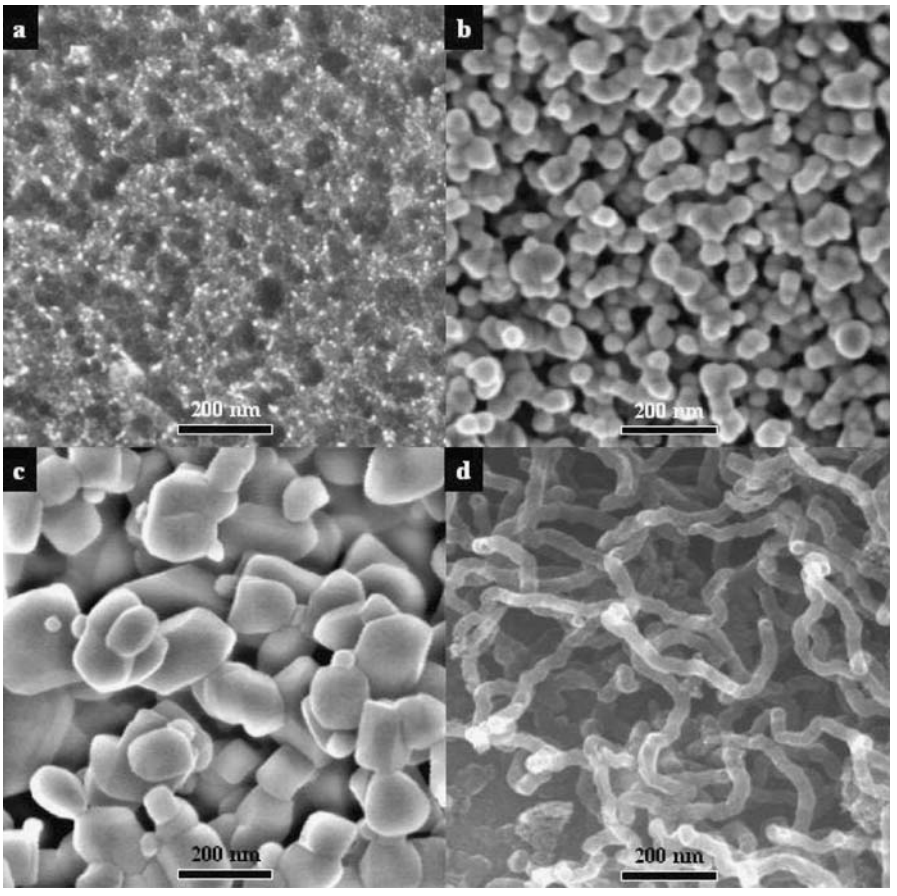

Figure 14. High-resolution SE images of (a) carbon supported Pt nanoparticle catalyst, (b) antimony-doped SnO_2 nanocrystals, (c) TiO_2 nanoparticles, and (d) carbon nanorods growing from a carbon substrate. These examples illustrate the powerful applications of high-resolution FEG-SEM to the characterization of various types of nanophase materials.

Other examples of applying high-resolution SEM imaging to the study of nanophase materials are shown in Fig. 14. Figure 14a shows a SE image of a carbon-supported Pt catalyst used in many catalytic chemical reactions. The image clearly provides information on the size and spatial distribution of the Pt nanoparticles; it also provides information on the pore structure of the carbon support as well as the spatial relationship between the Pt nanoparticles and the carbon pores. By varying the incident electron energy and by combining high-resolution SE imaging with BE imaging the three-dimensional distribution of the Pt nanoparticles may also be extracted. This type of information is invaluable for understanding the catalytic performance

of the supported catalyst, and for developing better nanostructured heterogeneous catalysts.

Figure 14b shows a high-resolution SE image of antimony-doped SnO_2 (ATO) nanoparticles. The ATO nanoparticles were developed for applications in sensors and smart devices, for example, electrochromic displays and windows. The information on the size distribution, the connectivity among, and the aggregation behavior of, the ATO nanoparticles is critical to optimizing the performance of the desired devices; the detailed pore structure of the ATO nano-powders is also critical to the optimization of electrochemical devices.

Figure 14c shows a high-resolution SE image of TiO_2 nanoparticles. These nanoparticles have important applications as pigments, as photo-catalysts, or as catalyst support materials; again, the size and shape distributions as well as the aggregation behavior of the TiO_2 nanoparticles are important parameters in determining their properties and applications. Tuning of the size distribution and the electronic structure of the TiO_2 nanoparticles determines the specific applications of these important semiconduting metal oxide nanoparticles.

Figure 14d shows clearly the shape and morphology of carbon nanorods as well as some extremely small metallic nanoparticles on the surfaces of these nanorods. This type of information can be effectively used to correlate the structure of the fabricated carbon nanophase materials to the synthesis processes. Carbon nanotubes and nanotube-based devices are in the forefront of nanoelectronics; and the ability to be able to statistically analyze large numbers of nanotubes or to be able to examine how these nanotubes interact with various substrates or other nanosystems is critically important.

In addition to the wide applications of high-resolution SEM to the semiconductor and nanoelectronics industries, the above examples clearly demonstrate the power of high-resolution SEM in solving challenging nanoscale materials problems.

7. SUMMARY AND PERSPECTIVES

In this chapter, we illustrated by using nanoparticles as a specific example the recent developments in SEM instrumentation and applications of high-resolution SEM to characterizing nanophase materials. High-resolution SEM techniques are now widely used in R&D laboratories, in manufacturing facilities, or in areas such as art, archeology, forensic investigations, environment preservation, etc.

At high electron energies, nanometer or subnanometer resolution SE images can now be routinely obtained in the new generation FEG-SEM instruments. To achieve the same image resolution at low electron energies, however, is still very challenging. As we discussed in section 3, both C_c and C_s aberration correctors have to be used to significantly reduce the effect of spherical and chromatic aberrations on the formation of low-energy electron nanoprobes. Such an attempt has already resulted in significant resolution improvement [39]. The use of aberration correctors not only makes the obtainable probe size much smaller but it makes possible to obtain high beam current contained within a small nanoprobe; high total beam current provides adequate

characteristic X-ray signals for chemical microanalysis or BE signals for high-quality, high-resolution imaging.

When the lens aberrations are corrected by using the aberration correctors, large probe-aperture angles have to be used, due to the diffraction limit, to obtain smaller probe sizes; the use of large probe-aperture angles significantly reduces the depth of field in SE images. However, we can effectively utilize this property to form confocal SEM images, similar to that of confocal laser scanning microscopy. The development of confocal SEM techniques will certainly make the high-resolution FEG-SEM technique much more powerful since true three-dimensional images of various samples can be obtained to provide not only the lateral but also the depth information on a nanometer scale.

For some samples, high probe current may be detrimental due to electron-beam induced irradiation damage of the sample; low probe current, however, usually results in poor signal-to-noise ratio and thus poor image or spectrum quality. Development of highly efficient detectors for both high-energy and low-energy electrons will prove to be fruitful in imaging and analyzing delicate samples. High-sensitivity BE detectors, especially at low-electron energies, are needed to differentiate phases that have small compositional differences. Use of SE and BE spectrometers in a modern FEG-SEM can further improve the image resolution and provide additional contrast. Energy-filtered SE and BE imaging will provide more detailed information on the samples of interest. It is possible that lattice fringes of bulk crystalline materials can be obtained in energy-filtered high-resolution BE images due to electron bean channeling effect.

The recent wide adoption of the environmental or variable pressure SEM instruments undoubtedly demonstrated the power of these microscopes. These microscopes can be operated as high-vacuum instruments or various gases can be allowed into the sample chamber to reduce sample-charging effects, to maintain low vapor pressure, or to study sample-gas interactions. It is anticipated that within a few years all the SEM instruments will be environmental or variable pressure SEM microscopes.

The recent development of ultra-low-voltage (ULV) imaging in the modern FEG-SEM is clearly interesting since this technique bridges the gap between SEM and low energy electron microscopy (LEEM) techniques. It is expected that different lens configurations will have to be used in order to achieve nanometer scale resolution with primary electron energies as low as a few eV. High-resolution ULV imaging makes it possible to reduce sample charging effect, to significantly reduce electron-induced damage of delicate samples, and to significantly increases surface sensitivity. For example, Fig. 15 shows a set of images obtained from the same region of a partially metallized polymer film. With the use of 500 eV electrons (Fig. 15a), the polymer film charged up and some of the metal particles appear dark in the image. With 100 eV electrons (Fig. 15b), the charging of the polymer film is significantly reduced and the metal particles appear bright now; but the contaminant in the center of the image was still charged up. When the electron energy was reduced to 50 eV or below, the image (Fig. 15c) clearly shows the sizes and morphology of the metal particles, the contaminant particle, and the surface details of the metal/polymer composites. Note

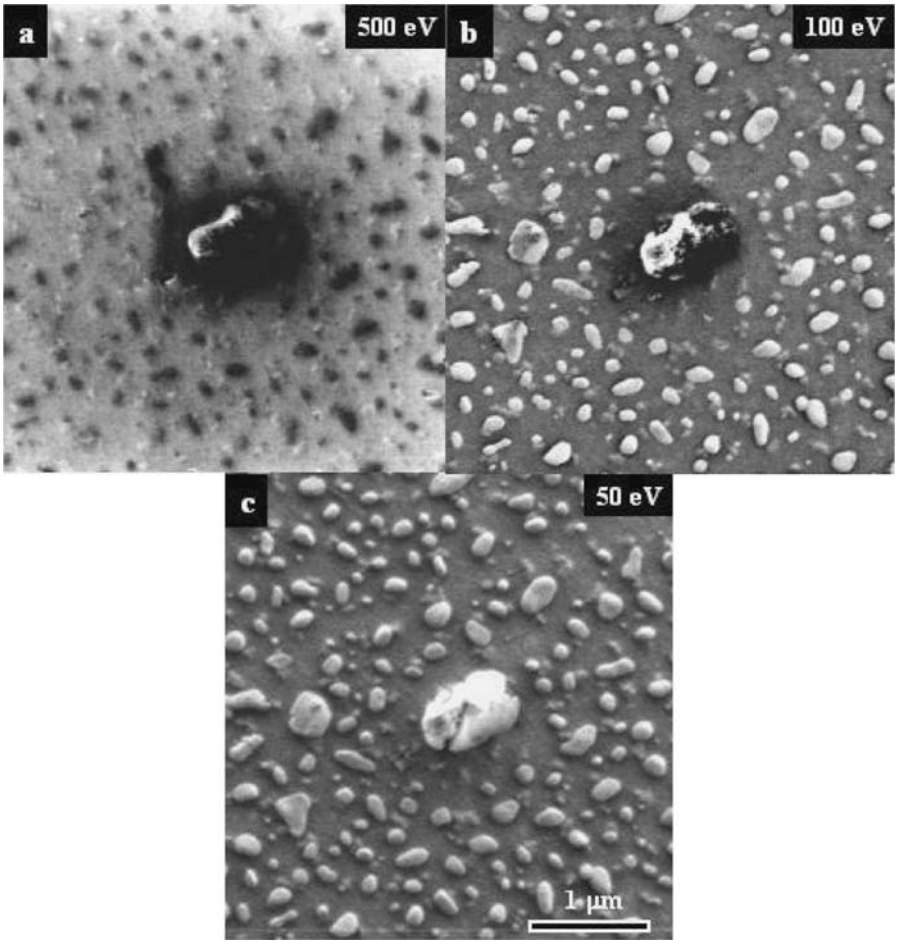

Figure 15. Low voltage (a, b) and ultra-low-voltage (c) SE images of a partially metallized polymer film illustrate the advantage of using low energy electrons. The Au particles are better revealed in images (b) and (c).

that the image resolution did not change much at all in all the images; high-resolution images can be obtained with primary electron energies <50 eV [23].

On the other hand, the recent development of ultra-high-voltage (~100 KV or above) SEM integrates the traditional SEM techniques to those of the STEM techniques; thus, both bulk samples and thin specimens can be examined by SEM techniques and TEM/STEM techniques can be applied to thin specimens. Subsurface structures can be revealed in high voltage SE or BE images. These microscopes are now broadly used in the semiconductor industry to characterize micro- or nano-devices.

The future generation electron microscopes may integrate all the functions that are now provided by SEM, TEM, and STEM techniques.

REFERENCES

1. M. Knoll, *Z. Tech. Phys.* 16 (1935) 497.
2. M. Von Ardenne, *Z. Phys.* 109 (1938) 553.
3. M. Von Ardenne, *Z. Tech. Phys.* 19 (1938) 407.
4. M. Knoll and R. Theile, *Z. Phys.* 113 (1939) 260.
5. V. K. Zworykin, J. Hillier, R. L. Snyder, *ASTM Bulletin* 117 (1942) 15.
6. C. W. Oatley, *J. Appl. Phys.* 53 (1982) R1.
7. A. V. Crew and J. Wall, *J. Mol. Biol.* 48 (1970) 373.
8. A. V. Crew, J. Wall and J. Langmore, *Science* 168 (1970) 1333.
9. A. V. Crew, *Rep. Progr. Phys.* 43 (1980) 621.
10. K.-R. Peters, *Scanning Electron Microscopy* 1982 (1982) 1359.
11. T. Nagatani, S. Saito, M. Sato, M.Yamada, *Scanning Microscopy* 1 (1987) 901.
12. D. Imeson, R. H. Milne, S. D. Berger, and D. McMullan, *Ultramicroscopy* 17 (1985) 243.
13. J. Liu and J. M. Colwey, *Ultramicroscopy* 23 (1987) 463.
14. J. Liu and J. M. Cowley, *Scanning Microscopy* 2 (1988) 63.
15. J. Liu and J. M. Cowley, *Scanning Microscopy* 2 (1988) 1957.
16. A. L. Bleloch, A. Howie and R. H. Milne, *Ultramicroscopy* 31 (1989) 99.
17. D. C. Joy and J. B. Pawley, *Ultramicroscopy* 47 (1992) 80.
18. A. Howie, *J. Microscopy* 180 (1995) 192.
19. R. Darji and A. Howie, *Micron* 28 (1997) 95.
20. J. Liu, *Microsc. Microanal.* 6 (2000) 388.
21. D. C. Joy and C. S. Joy, *Micron* 27 (1996) 247.
22. E. D. Boyes, *Adv. Mater.* 10 (1998) 1277.
23. J. Liu, *Mater. Characterization* 44 (2000) 353.
24. I. Mullerova and L. Frank, *Scanning* 15 (1993) 193.
25. J. Liu, *International Journal of Modern Physics* B16 (2002) 4387.
26. G. D. Danilatos, *Adv. Electron. El. Phys.* 71 (1988) 109.
27. P. J. R. Uwins, *Mater. Forum* 18 (1994) 51.
28. R. L. Schalek and L. T. Drzal, *Adv. Mater.* 32 (2000) 32.
29. A. M. Donald, *Nature Materials* 2 (2003) 511.
30. L. Reimer, *Scanning Electron Microscopy: Physics of Image Formation and Microanalysis*, Springer-Verlag, New York (1998).
31. J. I. Goldstein, D. E. Newbury, P. Echlin, D. C. Joy, A. D. Romig, Jr., C. E. Lyman, C. Fiori and E. Lifshin, *Scanning Electron Microscopy and X-Ray Microanalysis: A Text for Biologists, Materials Scientists, and Geologists*, Plenum, New York (1992).
32. D. C. Joy, *Monte Carlo Modeling for Electron Microscopy and Microanalysis*, Oxford University Press, New York (1995).
33. E. Bauer, *Rep. Prog. Phys.* 57 (1994) 895.
34. A. V. Crewe, J. Wall and L. M. Welter, *J. Appl. Phys.* 30 (1968) 5861.
35. V. E. Cosslett, *Optik* 36 (1972) 85.
36. J. Ximen, Z. Shao and P. S. D. Lin, *J. Microsc.* 170 (1993) 119.
37. A. V. Crewe, *Ultramicroscopy* 23 (1987) 159.
38. J. E. Barth and P. Kruit, *Optik* 101 (1996) 101.
39. J. Zach and M. Haider, *Nuclear Instruments and Methods in Physics Research* A363 (1995) 316.
40. M. Lenc and I. Mullerova, *Ultramicroscopy* 41 (1992) 411.
41. P. Kruit and G. H. Jansen, in *Handbook of Charged Particle Optics*, J. Orloff (Ed.), pp. 275–318, CRC Press, New York (1997).
42. Z. J. Ding and R. Shimizu, Scanning 18 (1996) 92.
43. J. Liu and J. M. Colwey, *Ultramicroscopy* 37 (1990) 50.
44. J. Drucker, M. R. Scheinfein, J. Liu and J. K. Weiss, *J. Appl. Phys.* 74 (1993) 7329.
45. H. Mullejans, A. L. Bleloch, A. Howie and M. Tomita, *Ultramicroscopy* 52 (1993) 360.
46. A. Howie, *J. Microscopy* 180 (1995) 192.
47. D. Imeson, *J. Microscopy* 147 (1987) 65.

48. J. Liu and J. M. Cowley, *Ultramicroscopy* 31 (1990) 119.
49. J. Liu and G. E. Spinnler, in: *Proceedings 50th Annual Meeting of EMSA* (1992), San Francisco Press, San Francisco, pp. 1288–1289.
50. J. Liu, R. L. Ornberg and J. R. Ebner, *Microscopy and Microanalysis, Vol. 3, Suppl. 2* (1997) 1123.
51. G. W. Jones and J. A. Venables (1985) *Ultramicroscopy* 18 (1985) 439.
52. J. A. Venables and J. Liu, in: *the Encyclopedia of Surface and Colloid Science*, A. P. Hubbard (Ed.), Marcel Dekker (2002).
53. Y. Homma, M. Suzuki, and M. Tomita, *Appl. Phys. Lett*. 62 (1993) 3276.
54. D. D. Perovic, M. R. Castell, A. Howie, C. Lavoie, T. Tiedje, and J. S. W. Cole, *Ultramicroscopy* 58 (1995) 104.
55. P. W. Tasker, *Adv. In Ceramics* 10 (1984) 176.